



Spreading dynamics of small river plumes off the northeastern coast of the Black Sea observed by Landsat 8 and Sentinel-2

Alexander Osadchiev*, Roman Sedakov

Shirshov Institute of Oceanology, Russian Academy of Sciences, Moscow, Russia

ARTICLE INFO

Keywords:

Surface currents
Small river plume
Coastal circulation
Coastal water quality
Optical flow
Motion detection
Optical satellite imagery
Black Sea
Mzymta River
Landsat 8
Sentinel-2

ABSTRACT

We use near simultaneous ocean color satellite imagery from NASA's Landsat 8 and ESA's Sentinel-2 missions to reconstruct surface currents along the northeastern shore of the Black Sea and study the spread of a small river plume formed in this area. Several times a year Landsat 8 and Sentinel-2 satellites both pass over the study area within a time interval of < 10 min. Analysis of near simultaneous ocean color composites obtained during these periods provides an opportunity for accurate reconstruction of surface currents. It is especially efficient for detecting motion of frontal zones associated with river plumes which are visible in optical satellite imagery. Using an optical flow algorithm we reconstructed surface currents associated with the motion of a small plume formed by the Mzymta River in response to different wind forcing conditions. We show that the dynamics of the Mzymta plume are significantly different to those of large plumes. First, a near-field jet of the small plume is abruptly decelerated by friction with the subjacent ocean and does not form a recirculating bulge even under low wind forcing conditions. As a result, freshwater discharge does not accumulate near the river mouth and is transported to the far-field part of the plume. Second, under certain external forcing conditions the angle between wind direction and Ekman transport within the plume takes anomalously large values of 60–80°. As a result, onshore winds cause upstream accumulation of the river plume, while offshore/downwelling and upwelling winds result in downstream and offshore transport of freshwater discharge, respectively.

1. Introduction

Buoyant river plumes are important features of the coastal sea in many world regions. Despite their relatively small surface areas and volumes as compared to the saline ambient sea they govern land-ocean fluxes of buoyancy, heat, terrigenous sediments, nutrients and anthropogenic pollutants and, thus, significantly influence many physical, biological, and geochemical processes on the continental shelf (e.g., Emmett et al., 2006; Milliman et al., 2007; Zhou et al., 2008; Rabalais, 2010; Huang et al., 2015; Osadchiev et al., 2017; Kubryakov et al., 2018). Structure, dynamics, and variability of river plumes are key factors for understanding mechanisms of advection, convection, transformation, accumulation and dissipation of fluvial discharge as well as suspended and dissolved river-borne constituents in the coastal sea (O'Donnell, 2010; Hetland and Hsu, 2013; Horner-Devine et al., 2015).

The processes of formation, spreading and mixing of river plumes are governed by two groups of factors. The first group consists of immanent characteristics of local landscapes, which include shoreline and seabed configurations, landforms and geographical disposition of river mouths, and latitude, which defines the local magnitude of the Coriolis

force (Chao and Boicort, 1986; Simpson, 1997; Horner-Devine et al., 2006; Warrick and Farnsworth, 2017). The second group consists of variable external forcing conditions, which include river discharge, local wind, coastal circulation, tides, waves, and stratification of the ambient ocean (O'Donnell, 1990; Fong and Geyer, 2001, 2002; Avicola and Huq, 2003; Yankovsky et al., 2001; Whitney and Garvine, 2005; Korotenko et al., 2014; Yuan et al., 2018; Osadchiev, 2018).

The structure and dynamics of a river plume strongly depend on its spatial scale, which varies in order of magnitude from a few meters to hundreds of kilometers due to over four orders of magnitude of variability of freshwater discharge rate among world river systems. Moreover, the size of an individual river plume can have significant intra-annual variability and, thus, diverse formation, spreading and mixing patterns within a year caused by inter-seasonal variability of river discharge rate (Geyer et al., 2000; Thomas and Weatherbee, 2006; Ostrander et al., 2008; Osadchiev et al., 2016; Osadchiev and Korshenko, 2017).

Many previous studies have addressed general aspects of the structure and dynamics of river plumes as well as their regional features. However, the majority of these works were focused on river

* Corresponding author.

E-mail address: osadchiev@ocean.ru (A. Osadchiev).

plumes formed by large and medium-size rivers and/or river plumes formed during high-discharge periods, while relatively little attention has been paid to small rivers plumes. This can be attributed to the small influence of individual small plumes on the coastal ocean as compared to large plumes. In addition, small plumes are characterized by very high temporal variability (of order of hours) in response to external forcing due to their small horizontal and vertical sizes. This fact hinders precise measurements of their circulation patterns and mixing mechanisms. Yet, the total share of small rivers influxes of fluvial water and suspended sediments to the world ocean is estimated at about 25% and 40%, respectively (Milliman and Syvitski, 1992; Milliman et al., 1999). Furthermore, this contribution is much more significant on a regional scale for many coastal regions.

In this work we focus on the buoyant plume formed by the Mzymta River, a small river at the northeastern part of the Black Sea. We study the dynamics of this river plume based on satellite imagery from NASA's Landsat 8 and ESA's Sentinel-2 missions. Both missions provide global coverage with a 5-day repeat cycle for Sentinel-2 (which was equal to 10 days before Sentinel-2B was launched in March 2017) and a 16-day repeat cycle for Landsat 8. The orbital paths of Sentinel-2 and Landsat 8 intersect at some points with small time intervals ($< 10\text{--}15$ min). As a result, since June 2015, when the Sentinel-2 mission started and especially since March 2017 when Sentinel-2B was launched, some world areas are regularly observed by Sentinel-2 Multi Spectral Instrument (MSI) and Landsat 8 Operational Land Imager (OLI) sensors nearly simultaneously and with similar view angles (Li and Roy, 2017). One of these areas covers the northeastern coast of the Black Sea including the area adjacent to the Mzymta mouth (Fig. 1). In this work we used near simultaneous images of this area taken by Sentinel-2 and Landsat 8 during nine cloud-free days in 2016–2018.

Many previous works have focused on reconstruction of sea surface currents from optical, near-infrared, and thermal-infrared satellite imagery using maximum cross correlation (MCC) method (Emery et al., 1986, 1992; Bannehr et al., 1996; Domingues et al., 2000; Zavialov et al., 2002; Bowen et al., 2002; Matthews and Emery, 2009; Mercatini et al., 2010) and optical flow (Bannehr et al., 1996; Sun et al., 2016) algorithms. However, as time spans between pairs of analyzed satellite images in most of these studies were of order of days this negatively affected the accuracy of the applied motion detection algorithms. In particular, it resulted in low efficiency of reconstruction of surface currents related to motion of highly variable sub-mesoscale ocean

structures including buoyant river plumes (Marcello et al., 2008; Chen, 2011). In the last several years a number of relevant studies used satellite images from Geostationary Ocean Color Imager (GOCI), a geostationary satellite, which has an observational interval of order of hours, but relatively low spatial resolution (500 m) (Yang et al., 2014, 2015; Hu et al., 2016; Sun et al., 2016). Geostationary satellites also have limited spatial coverage and cannot be used for reconstruction of surface currents in temperate and polar latitudes.

In this work we present a new approach that is based on near simultaneous Sentinel-2 and Landsat 8 measurements, which has potential to provide accurate detection of surface currents in many world regions. Sharp frontal zones associated with river plumes in general are distinctly visible on medium resolution ocean color composites from Sentinel-2 (10 m) and Landsat 8 (30 m). Thus, satellite observations captured with small time intervals (of order of minutes) provide the opportunity for precise detection of small frontal shifts, while general frontal patterns do not change. Therefore, a surface velocity field associated with motion of a plume can be accurately reconstructed by a calibrated motion detection algorithm applied to near simultaneous satellite images. The main drawback of this approach is low temporal coverage and a dependence on cloud-free conditions at the time of image capture. However, this method can be extremely useful for studying surface processes with significant spatial and temporal variability that require instantaneous measurements of surface currents with high spatial resolution, in regions where in situ measurements are not feasible.

The paper is organized as follows. Section 2 provides detailed information about the study area, the Sentinel-2 and Landsat 8 satellite data and in situ data used in this study, and the optical flow algorithm applied for motion detection. The results of reconstruction of surface currents within the Mzymta plume from near simultaneous satellite images and analysis of characteristics of frontal zones of the Mzymta plume observed in the satellite imagery are described in Section 3. Section 4 focuses on physical interpretation of the reconstructed spreading dynamics of a small river plume under various external forcing conditions. Summary and conclusions are given in Section 5.

2. Data and methods

2.1. Study region

In this work we focus on the Mzymta plume formed in the northeastern part of the Black Sea (Fig. 1). The average annual discharge of the Mzymta River is approximately $50\text{ m}^3/\text{s}$ with a drought period in autumn and winter and a freshet in spring and early summer associated with snow melting (Jaoshvili, 2002; Alexeevsky et al., 2016). The Mzymta River forms a buoyant plume with small horizontal (< 10 km) and vertical (< 4 m) dimensions. It results in a quick response of the Mzymta plume to the highly variable river discharge rate and wind forcing revealed by in situ and satellite measurements (Korotkina et al., 2011, 2014; Osadchiv and Zavialov, 2013). The continental shelf at the study area is very steep and narrow; therefore, the Mzymta plume does not exhibit friction with the sea bottom. Tidal amplitudes at the study area are < 6 cm; thus, tidal circulation does not significantly influence the Mzymta plume (Medvedev et al., 2016; Medvedev, 2018). The annual average concentration of suspended sediments in the discharge of the Mzymta River is 165 g m^{-3} (Jaoshvili, 2002). As a result, the turbid Mzymta plume can be effectively detected by optical satellite imagery, as was addressed in Zavialov et al. (2014) and Osadchiv (2015).

2.2. Satellite and in situ data

Spreading dynamics of the Mzymta plume were studied using Sentinel-2 MSI and Landsat 8 OLI data collected in 2013–2018 with emphasis on nine near simultaneous pairs of Sentinel-2 and Landsat 8

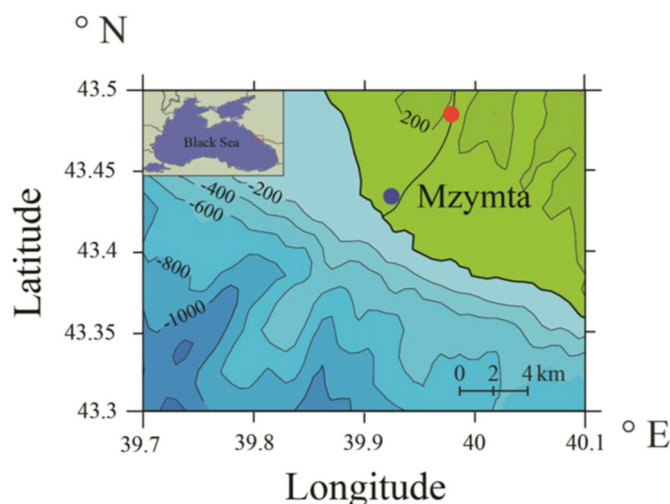


Fig. 1. Bathymetry and topography of the study region, locations of the Adler airport meteorological station (blue circle) and the Kazachiy Brod gauge station (red circle). Location of the study region at the northeastern part of the Black Sea is shown in the inset. (For interpretation of the references to color in this figure legend, the reader is referred to the web version of this article.)

Table 1
Observation times and difference in capture times between the analyzed near simultaneous pairs of Sentinel-2 and Landsat 8 ocean color composites.

Date	Landsat 8 observation time	Sentinel-2 observation time	Time difference
23.04.2016	8:07:26	8:14:36	0:07:10
12.07.2016	8:07:51	8:10:13	0:02:22
30.09.2016	8:08:09	8:13:38	0:05:29
9.03.2017	8:07:42	8:14:38	0:06:56
28.05.2017	8:07:29	8:10:43	0:03:14
10.09.2017	8:01:51	8:09:59	0:08:08
17.02.2018	8:01:32	8:10:09	0:08:37
12.03.2018	8:07:31	8:17:29	0:09:58
6.04.2018	8:01:08	8:16:01	0:14:53

images acquired on 23 April, 12 July, 30 September 2016, 9 March, 28 May, 10 September 2017, 17 February, 12 March, and 6 April 2018. Observation times of these satellite images and difference in capture times are given in Table 1.

The Landsat 8 Surface Reflectance Level-2 products were downloaded from the United States Geological Survey web repository (<http://earthexplorer.usgs.gov>). The Sentinel-2 Level-1C products were downloaded from the Copernicus Open Access Hub (<https://scihub.copernicus.eu/>). Atmospheric correction was applied to these products using Sen2Cor module version 2.2.1 within the Sentinel-2 Toolbox (S2TBX), Sentinel Application Platform (SNAP) version 5.0.7. Due to a misregistration issue of Sentinel-2 and Landsat 8 imagery reported by Storey et al. (2016) the residual difference between the near simultaneous pairs of ocean color composites is equal to 25 m which is more than two Sentinel-2 10-meter pixels. Also processing of the near simultaneous pairs of satellite images by motion detection algorithms requires their resampling to a common pixel resolution. Therefore, we improved alignment between these pairs of images and resampled them to a common pixel resolution by manually identifying several control points at the study region (buildings and piers) and downsampling Sentinel-2 ocean color composites (10 m) to spatial resolution of Landsat 8 ocean color composites (30 m) using bilinear algorithm.

The Mzymta discharge and local wind forcing data was used to study the influence of external forcing conditions on dynamics of the Mzymta plume. The Mzymta discharge data was obtained from the Kazachiy Brod gauge station, while local wind measurements were performed at the Adler airport meteorological station located 2 km far from the Mzymta mouth at the altitude of 27 m (Fig. 1).

2.3. Motion detection algorithms

Velocity fields in the ocean surface layer addressed in this study were retrieved from satellite imagery using computer vision techniques, namely, optical flow approach. Optical flow estimation is one of the oldest branches of the computer vision and has been actively developed during recent decades (e.g., Baker et al., 2011; Fortun et al., 2015). In the last several years optical flow algorithms have been applied to satellite imagery for various geoscientific applications including ocean circulation (Sun et al., 2016), sea ice drift (Petrou and Tian, 2017), cloud motion (Wu et al., 2016), and glacier flow estimation (Altena and Kaab, 2017; Lenzano et al., 2018). However, the number of relevant studies is still relatively small despite the great potential of optical flow algorithms in reconstruction of motion vector fields.

The main principle of optical flow algorithms used for calculation of motion from two consecutive pictures is the following. It is assumed that for each point \vec{x} (i.e., pixel) on both frames a certain signal intensity property I (i.e., brightness) is conserved: $I(\vec{x}, t) = I(\vec{x} + \Delta\vec{x}, t + \Delta t)$. By linearizing the intensity of the second frame with respect to the intensity of the first frame a gradient constraint equation is obtained in the following way: $\nabla I(\vec{x}, t) \cdot \vec{u} + I_t(\vec{x}, t) = 0$, where $\nabla I = (I_x, I_y)$ is the spatial partial

derivatives of intensity, $\vec{u} = d\vec{x}/dt$ is the velocity, I_t is the temporal derivative of intensity. The derivatives ∇I and I_t can be directly calculated, while the 2D velocity field \vec{u} is unknown. Therefore, this equation requires an additional constraint and it is assumed that the displacement $\Delta\vec{x}$ is constant in any small neighborhood, i.e., we search for a displacement that minimizes the constraint error $E(\vec{x}) = \sum_{\vec{x}} g(\vec{x})(\nabla I(\vec{x}, t) \cdot \vec{u} + I_t(\vec{x}, t))^2$, where $g(\vec{x})$ is a weight function. Thus, minimization of $E(\vec{x})$ with respect to \vec{u} provides an additional condition for gradient constraint equation. The resulting vector field \vec{u} calculated from these two equations is regarded as an optical flow estimate. Optical flow algorithms operate with gradients of signal intensity; therefore their results are not sensitive to relative variations of surface reflectance within processed images. As a result, differences in atmospheric correction of Landsat 8 and Sentinel-2 satellite data do not hinder application of optical flow algorithms for motion detection, as long as both images are in the same relative scale.

In this work we compared three optical flow algorithms with different weight functions, namely, Lucas and Kanade (1981), Horn and Schunck (1981), and Farneback (2003) algorithms. Quality analysis of results obtained by the three optical flow algorithms was based on, first, general accordance between current shapes and visually inspected shifts of frontal zones at consecutive satellite images, and, second, the number of implausible vectors and continuity of currents. In general, the Farneback algorithm captured more accurately both small and large displacements and provided the most realistic optical flow estimations for the analyzed satellite imagery. This algorithm approximates a neighborhood of a pixel in each pair of frames by a quadratic polynomial function applying the polynomial expansion transform. Thus, a constraint equation is based on a polynomial approximation of the given signal. On the assumption of small variability of a displacement field, the algorithm minimizes quadratic error of the constraint and calculates the optical flow estimation. Estimation of surface velocity fields in the study region was performed in two stages. First, we applied the Farneback optical flow algorithm with large prescribed sizes of pixel neighborhood for the reconstruction of motion of distinct plume boundaries and fronts. Second, we reconstructed motion within the river plume using the optical flow algorithm with a reduced neighborhood size. The resulting velocity field was smoothed by an averaging filter using the surface velocity field obtained at the first stage as a skeleton.

Spatial scale of motion, which is intended to be reconstructed, positively correlates with optimal size of a pixel neighborhood. An algorithm with a small pixel neighborhood more accurately reconstructs small-scale motion, but shows lower quality for large motion patterns, as compared to algorithm with a large pixel neighborhood. The overall neighborhood size is prescribed according to spatial scales of ocean surface features (e.g., river plume fronts), which motion is expected to be detected by optical flow algorithm. Thus, optimal neighborhood size intended to reconstruct large-scale motion of river plumes should be equal to width of distinct plume boundaries and fronts. In this study, large size of a pixel neighborhood was prescribed equal to 5 pixels (150 m). On the other hand, neighborhood size is limited by spatial resolution of the analyzed satellite imagery. Therefore, small size of a pixel neighborhood was set equal to 1 pixel (30 m). Values of neighborhood sizes were fixed for all pairs of analyzed satellite imagery due to low variability of spatial extents of the Mzymta plume. In case of application of this algorithm to other regions, we suggest prescribing neighborhood sizes equal to relevant spatial scales of considered ocean surface features. However, many specific aspects of this issue (dependence between optimal neighborhood size and motion spatial scale, accuracy, sensitivity, computational efficiency, etc.) require a detailed study and are beyond the scope of the current work.

At both stages we obtained velocity vectors, which reproduced movement of clouds in the sky and vessels in the sea and were not related to surface water flow. These vectors have significantly different

Table 2

Local wind forcing, the Mzymta discharge rate during the considered periods and their climatological mean monthly values and standard deviations.

Date	Mzymta discharge, m ³ /s	Mean value and standard deviation of monthly Mzymta discharge, m ³ /s	Wind direction	Wind speed, m/s	Mean value and standard deviation of monthly wind speed, m/s
23.04.2016	118	90.4 ± 21.6	SW (onshore)	3	3.0 ± 1.4
12.07.2016	59	48.5 ± 19.3	SE (downwelling)	4	3.2 ± 1.1
30.09.2016	70	19.2 ± 11.0	N (upwelling)	2	3.4 ± 1.3
9.03.2017	75	49.8 ± 11.9	0	0	3.1 ± 1.3
28.05.2017	115	107.0 ± 21.2	S (downwelling)	4	2.7 ± 1.2
10.09.2017	44	19.2 ± 11.0	0	0	3.4 ± 1.3
17.02.2018	41	36.6 ± 7.7	SW (onshore)	3	3.3 ± 1.4
12.03.2018	94	49.8 ± 11.9	SW (onshore)	3	3.1 ± 1.3
6.04.2018	96	90.4 ± 21.6	SW (onshore)	3	3.0 ± 1.4

motion characteristics, as compared to vectors related to sea surface circulation. These false vectors were manually identified and removed from the resulting velocity fields of nine pairs of near simultaneous satellite images. However, for a larger dataset, or for cases with many potential sources of aliasing (mainly ships and clouds, but also fog, dust and smoke, planes, birds, large sea mammals, etc.) automated detection and removal of non-circulation-related features could be applied.

3. Results

3.1. Surface currents

The optical flow processing of near simultaneous Landsat 8 and Sentinel-2 ocean color composites revealed surface velocity field associated with spreading of the Mzymta plume on 23 April, 12 July, 30 September 2016, 9 March, 28 May, 10 September 2017, and 12 March 2018. Diverse wind and discharge conditions occurred during the considered periods (Table 2) resulting in significantly different spatial extents and motion patterns of the Mzymta plume.

The spreading pattern of the Mzymta plume under calm wind forcing conditions was observed on 9 March 2017 and 10 September 2017 (Fig. 2). The near-field part of the Mzymta plume spread radially from the river mouth, decelerated, and rotated clockwise approximately 2 km from the river mouth. The anticyclonic flow formed along the edge of the semi-circular near-field plume transitioned to an alongshore current propagated northwestward from the Mzymta mouth (hereinafter referred as downstream alongshore direction). Thus, the near-field plume did not form an anticyclonic recirculation bulge adjacent to the river mouth, which is typical for river plumes under low wind forcing conditions as identified in a number of theoretical (Yankovsky and Chapman, 1997), in situ (Chant et al., 2008; Horner-Devine, 2009; Kudela et al., 2010), laboratory (Avicola and Huq, 2003; Horner-Devine et al., 2006; Thomas and Linden, 2007; Yuan et al., 2018), and

numerical (Fong and Geyer, 2002; Whitney and Garvine, 2005; Soosaar et al., 2016) studies. A sharp front formed between the Mzymta plume and the ambient sea was distinctly visible in the optical satellite imagery. It extended from the coast at a distance of 3 km to southeast from the Mzymta mouth (hereinafter referred as upstream alongshore direction), contoured the near-field plume, and propagated approximately 6 km downstream where the strong gradient between the far-field plume and the ambient ocean decayed. The Mzymta discharge rate on 9 March 2017 was low (75 m³/s), however, the distance between the plume front and the shore was 3–5 km, while the alongshore extent of the far-field geostrophic current was approximately 7–8 km.

Moderate southerly and southeasterly winds (4 m/s) dominated in the study area during satellite observations on 12 July 2016 and 28 May 2017 and induced similar spreading patterns of the Mzymta plume (Fig. 3). The near-field plume jet decelerated on a distance of 0.5–1 km from the Mzymta mouth, rotated clockwise, and transformed into the far-field plume. The far-field plume was spreading northward along the shore in response to downwelling favorable wind forcing. As a result, the sharp front of the Mzymta plume originated from the coast < 1 km upstream from the Mzymta mouth and was stretched downstream. The Mzymta discharge rate on 28 May 2017 was two times greater than on 12 July 2016, which resulted in difference in offshore shifts of the alongshore front of the Mzymta plume (3 km and 1 km, respectively). Downstream alongshore extents of the far-field plume were 8–10 km for both discharge conditions.

Spreading pattern of the Mzymta plume under upwelling favorable winds (2 m/s) observed on 30 September 2016 is characterized by large offshore spreading of the near-field plume, its subsequent clockwise rotation and transition to the far-field plume (Fig. 4). The sharp cross-shore front between the near-field plume and the ambient sea was formed approximately 1.5 km upstream from the Mzymta mouth and was stretched in a westerly direction. The far-field plume spread northwestward and covered a large coastal area (exceeding 50 km²)

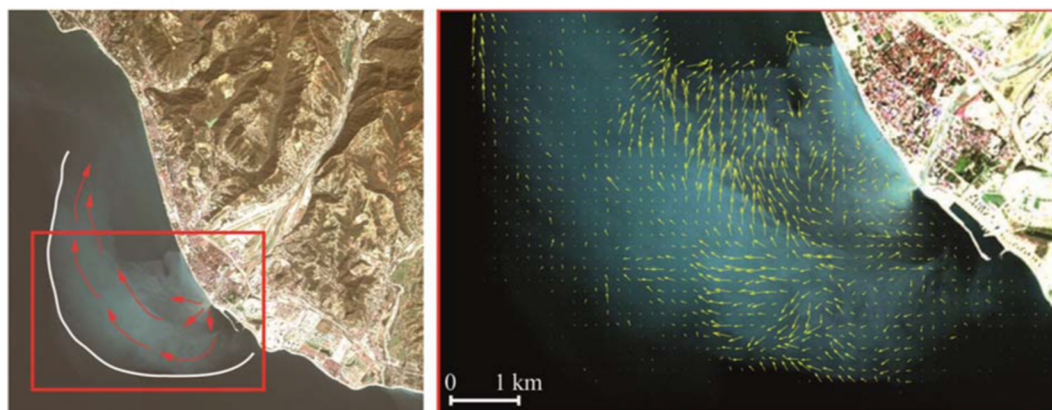


Fig. 2. Sentinel-2 ocean color composite from 9 March 2017, plume spreading scheme (left), and surface velocity field within the Mzymta plume (right) reconstructed by the optical flow algorithm. The white line reproduces the sharp front between the plume and ambient sea.

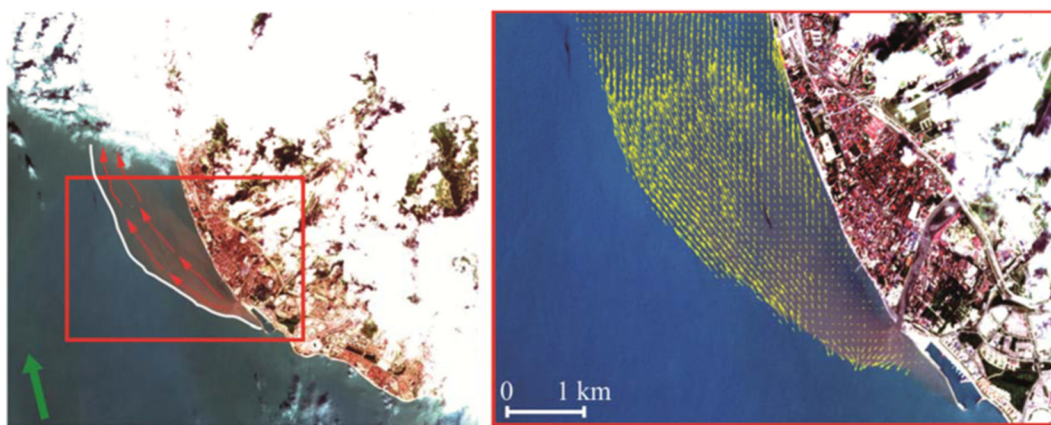


Fig. 3. Sentinel-2 ocean color composites from 28 May 2017, plume spreading scheme (left), and surface velocity field within the Mzymta plume (right) reconstructed by the optical flow algorithm. The white line reproduces the sharp front between the plume and ambient sea, the green arrow indicates wind direction. (For interpretation of the references to color in this figure legend, the reader is referred to the web version of this article.)

despite the relatively low river discharge rate of the Mzymta River ($70 \text{ m}^3/\text{s}$). The longshore scale of the far-field plume was $> 15 \text{ km}$. The distance between the alongshore front of the far-field plume and the shoreline increased from 4 km near the river mouth to 6–8 km in its downstream part.

The spreading of the Mzymta plume in response to light southwesterly winds (3 m/s) was reconstructed from satellite imagery acquired on 23 April 2016, 17 February 2018, 12 March 2018, and 6 April 2018 (Fig. 5). During these days the near-field jet was propagating southward and southeastward from the Mzymta mouth for distances of 1–2 km. Then the near-field jet rotated counterclockwise and transformed into the far-field plume, which spread upstream with decaying velocity. As a result, onshore winds arrested the far-field plume near the shore and an upstream alongshore current did not form. Despite high discharge rates of the Mzymta River on 23 April 2016 ($118 \text{ m}^3/\text{s}$), 12 March 2018 ($94 \text{ m}^3/\text{s}$), and 6 April 2018 ($96 \text{ m}^3/\text{s}$) alongshore extents of the Mzymta plume were only 5–6 km, respectively, while during the low discharge period observed on 17 February 2018 ($41 \text{ m}^3/\text{s}$) the plume alongshore extent was 1 km. The Mzymta plume accumulated upstream of the Mzymta mouth was contoured by the sharp plume front, which originated downstream from the Mzymta mouth.

3.2. Plume fronts

The shape of a small river plume and its location in relation to a river mouth and a coastline are indicative of surface circulation

patterns within a plume. A small river plume generally has two types of frontal zones between freshened plume waters and ambient sea, namely, diffuse and sharp fronts (Bowman and Iverson, 1978; Jay et al., 2009; Devlin and Pan, 2017). A diffuse frontal zone, which is relatively wide and is characterized by low salinity gradients, contours outer parts of the plume, which exhibits intense mixing with ambient sea. If a small plume is spreading in response to wind forcing and plume mixing is induced by velocity shear between a plume and subjacent sea, a diffuse frontal zone is formed “in front” of a spreading plume. A sharp frontal zone, in contrast, is narrow (up to order of tens of centimeters), is characterized by strong gradients and, therefore, is often distinctly visible in satellite imagery. This frontal zone indicates the outer parts of the plume, which exhibit low mixing with ambient sea and are generally formed “behind” a spreading plume. In particular, the flow lines of a plume circulation do not cross sharp fronts between the plume and ambient sea (Bowman and Iverson, 1978; O'Donnell, 2010; Horner-Devine et al., 2015). Therefore, flow velocities near a sharp plume border are generally directed along its frontline, while the motion velocity of a front itself is significantly lower (O'Donnell et al., 1998, 2008; Trump and Marmorino, 2003).

In this study, frontal boundaries of the Mzymta plume were identified basing on visual inspection of the color composite imagery due to generally strong color contrast between river plume and ambient sea at the study region (Osadchiev and Zavialov, 2013; Zavialov et al., 2014). However, color algorithms can be applied for automation of frontal detection in case of a larger dataset, or for regions with low color

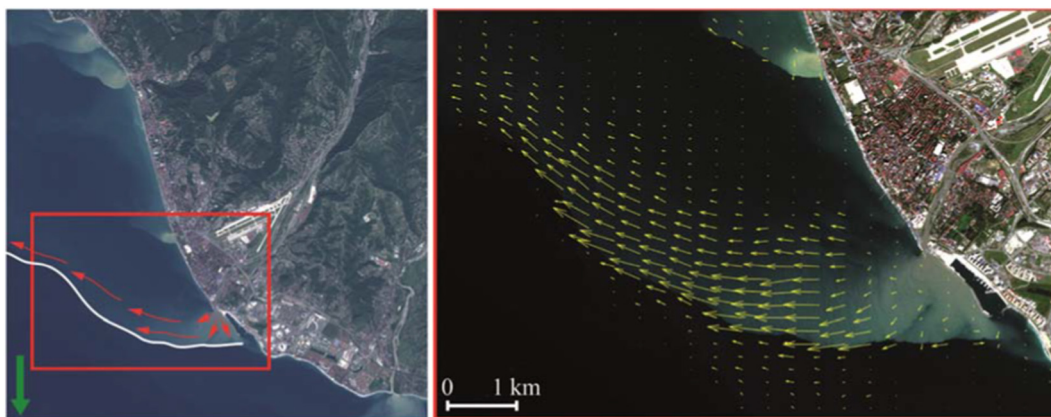


Fig. 4. Sentinel-2 ocean color composite from 30 September 2016, plume spreading scheme (left), and surface velocity field within the Mzymta plume (right) reconstructed by the optical flow algorithm. The white line reproduces the sharp front between the plume and ambient sea, the green arrow indicates wind direction. (For interpretation of the references to color in this figure legend, the reader is referred to the web version of this article.)



Fig. 5. Sentinel-2 ocean color composites from 12 March 2018, plume spreading scheme (left), and surface velocity field within the Mzymta plume (right) reconstructed by the optical flow algorithm. The white line reproduces the sharp front between the plume and ambient sea, the green arrow indicates wind direction. (For interpretation of the references to color in this figure legend, the reader is referred to the web version of this article.)

contrasts between river plumes and ambient sea. The locations and shapes of the sharp frontal zones of the Mzymta plume visually observed in satellite imagery are in good agreement with surface velocity fields calculated by the optical flow algorithm and described in Section 3.1. Thus, they confirm the reconstructed spreading patterns of the Mzymta plume in response to different types of wind forcing. In particular, the sharp frontal zone observed in the vicinity of the Mzymta mouth on 30 September 2016 was located upstream the river mouth and was stretched westward indicating offshore flow in the upstream part of the Mzymta plume and general downstream transport of freshened water under upwelling wind forcing (Fig. 4). The sharp fronts of the Mzymta plume observed on 23 April 2016, 12 March 2018, and 6 April 2018 during onshore winds were also stretched in the cross-shore direction but were located downstream of the river mouth indicating offshore flow in the downstream part of the Mzymta plume and general upstream transport of freshened water under onshore wind forcing (Fig. 5).

Based on non-coincident Landsat 8 and Sentinel-2 imagery acquired during 96 cloud-free periods in 2013–2018 we visually identified sharp frontal zones of the Mzymta plume under various wind and discharge conditions (Table 3). Dependence of locations and forms of the sharp fronts of the plume on the direction of local wind forcing showed very good accordance with spreading patterns of the Mzymta plume identified by near simultaneous satellite imagery and described in Section 3.1. In particular, downstream location of the sharp plume front and upstream accumulation of the Mzymta plume was observed only during onshore winds, hereinafter referred as the upstream spreading winds. All other types of wind forcing including calm wind conditions, hereinafter referred as the downstream spreading winds, resulted in upstream location of the sharp plume front and downstream spreading of the plume. However, in several cases onshore winds were accompanied by upstream location of the sharp plume front. This feature was registered when downstream spreading winds changed to onshore winds shortly before the observation period. Therefore, we assume that in these cases onshore winds induced upstream spreading of the Mzymta plume, but sharp downstream plume front did not formed yet at the observation moment due to preceding downstream spreading of the plume.

An upstream location of the sharp front of the Mzymta plume and downstream spreading of the plume was observed during periods of offshore winds, which influence on plume spreading was not revealed by the available near simultaneous Landsat 8 and Sentinel-2 imagery. A typical form of the Mzymta plume under northeasterly wind forcing (2 m/s) was observed on 27 July 2017 (Fig. 6). The cross-shore extent of the Mzymta plume formed by relatively low discharge (57 m³/s) on 27

July 2017 during offshore winds (1.5 km) was much smaller than during upwelling winds on 30 September 2016 (70 m³/s, exceeding 15 km), but larger than during downwelling winds on 27 July 2017 (59 m³/s, 1 km).

4. Discussion

Based on the results described in Section 3, we suggest a dynamical interpretation of the reconstructed spreading patterns of the Mzymta plume under different wind forcing conditions. These spreading patterns showed significant difference from those typical for medium-size and large rivers (e.g., Yankovsky and Chapman, 1997; Nof and Pichevin, 2001; Fong and Geyer, 2002; Horner-Devine et al., 2006; MacDonald et al., 2007; Chant et al., 2008; Liu et al., 2009). The main distinctions of the observed dynamics of the Mzymta plume are the following: First, the near-field part of the Mzymta plume is of one order of magnitude smaller than it is estimated by widely used parameterizations of spatial scales of a near-field plume based on river discharge parameters. Second, the near-field freshened jet does not form a mid-field plume, i.e., a recirculating bulge adjacent to the river mouth, which is a typical feature of a river plume under low wind forcing conditions. The near-field plume directly transitions to the wind-dominated or geostrophic far-field plume within a distance of 1–2 km from the Mzymta mouth. Finally, the wind-induced Ekman transport within the Mzymta plume occurs at a wide range of angles to wind direction during upwelling, onshore, and offshore wind forcing periods. It decreases from anomalously large values of 60–80° in vicinity of the Mzymta mouth to 30–40° at the outer parts of the plume. Below we provide and discuss the physical interpretation of these dynamical features of the Mzymta plume.

In this study we focus on wind as a primary external force that governs spreading dynamics of the Mzymta plume. We pay low attention to river discharge rate and do not consider local coastal circulation due to the following reasons. Large synoptic and seasonal variability of discharge rate (1–2 orders of magnitude) typical for small rivers strongly affects structure and dynamics of river plumes (Warrick et al., 2004; Nezlin and DiGiacomo, 2005; Nezlin et al., 2005; Warrick et al., 2007; Saldias et al., 2012; Romero et al., 2016). However, in the current study we analyze dynamics of the Mzymta plume within relatively small range of variability of river discharge rate, i.e., from 41 to 118 m³/s (Table 2). In this case spreading patterns of the Mzymta plume are governed mainly by wind forcing which was shown by Osadchiv and Zavialov (2013). Coastal circulation also can influence dynamics of a river plume (Fong and Geyer, 2002), however, several works showed that its impact on small plumes (Washburn et al., 2003;

Table 3

Local wind forcing, location of the sharp front of the Mzymta plume, and plume spreading type during cloud-free periods at the study region in 2013–2018 detected by Landsat 8 and Sentinel-2. Upstream front and downstream front are referred as UF and DF, respectively; downstream plume spreading and upstream plume accumulation are referred as DS and UA, respectively.

Satellite	Date	Wind direction and type	Wind speed, m/s	Location of the sharp plume front	Plume spreading type
Sentinel-2	10.10.2018	N (upwelling)	2	UF	DS
Sentinel-2	08.10.2018	N (upwelling)	2	UF	DS
Sentinel-2	05.10.2018	NW (upwelling)	4	UF	DS
Sentinel-2	25.09.2018	NW (upwelling)	2	UF	DS
Landsat 8	20.09.2018	0	0	UF	DS
Sentinel-2	18.09.2018	S	3	UF	DS
Sentinel-2	15.09.2018	(downwelling)			
Sentinel-2	15.09.2018	SW (onshore)	3	DF	UA
Sentinel-2	03.09.2018	S	3	UF	DS
Sentinel-2	16.05.2018	(downwelling)			
Sentinel-2	16.05.2018	S	3	UF	DS
Sentinel-2	03.05.2018	(downwelling)			
Sentinel-2	03.05.2018	SW (onshore)	4	DF	UA
Sentinel-2	01.05.2018	W (onshore)	4	DF	UA
Sentinel-2	23.04.2018	SE	5	UF	DS
Sentinel-2	16.04.2018	(downwelling)			
Sentinel-2	16.04.2018	SE	7	UF	DS
Sentinel-2	11.04.2018	(downwelling)			
Sentinel-2	11.04.2018	SW (onshore)	4	DF	UA
Sentinel-2	01.04.2018	SE	5	UF	DS
Landsat 8	21.03.2018	(downwelling)			
Landsat 8	21.03.2018	SW (onshore)	4	DF	UA
Sentinel-2	17.03.2018	SE	7	UF	DS
Sentinel-2	07.03.2018	(downwelling)			
Sentinel-2	07.03.2018	SE	7	UF	DS
Sentinel-2	10.02.2018	(downwelling)			
Sentinel-2	10.02.2018	SW (onshore)	1	DF	UA
Sentinel-2	07.02.2018	0	0	UF	DS
Landsat 8	01.02.2018	NE (offshore)	5	UF	DS
Sentinel-2	11.01.2018	E, offshore	1	UF	DS
Sentinel-2	08.01.2018	E, offshore	3	UF	DS
Landsat 8	07.01.2018	NE (offshore)	4	UF	DS
Sentinel-2	24.12.2017	NW (upwelling)	4	UF	DS
Sentinel-2	14.12.2017	NE (offshore)	4	UF	DS
Sentinel-2	12.12.2017	NE (offshore)	6	UF	DS
Sentinel-2	04.12.2017	SE	2	UF	DS
Sentinel-2	02.12.2017	(downwelling)			
Sentinel-2	02.12.2017	E, offshore	3	UF	DS
Sentinel-2	17.11.2017	NE (offshore)	2	UF	DS
Sentinel-2	9.11.2017	E, offshore	1	UF	DS
Sentinel-2	25.10.2017	E, offshore	3	UF	DS
Sentinel-2	30.09.2017	W (onshore)	3	UF	DS
Landsat 8	26.09.2017	W (onshore)	3	UF	DS
Sentinel-2	25.09.2017	S	3	UF	DS
Sentinel-2	15.09.2017	(downwelling)			
Sentinel-2	15.09.2017	W (onshore)	2	DF	UA
Sentinel-2	08.09.2017	S	2	UF	DS
Sentinel-2	05.09.2017	(downwelling)			
Sentinel-2	05.09.2017	S	3	UF	DS
Sentinel-2	21.08.2017	(downwelling)			
Sentinel-2	21.08.2017	SW (onshore)	3	UF	DS
Sentinel-2	19.08.2017	W (onshore)	3	UF	DS
Sentinel-2	01.08.2017	S	3	UF	DS
Sentinel-2	27.07.2017	(downwelling)			
Sentinel-2	27.07.2017	NE (offshore)	2	UF	DS
Sentinel-2	25.07.2017	N (upwelling)	2	UF	DS
Landsat 8	24.07.2017	S	4	UF	DS
Sentinel-2	22.07.2017	(downwelling)			
Sentinel-2	22.07.2017	W (onshore)	3	UF	DS
Sentinel-2	12.07.2017	S	4	UF	DS
Sentinel-2	10.07.2017	(downwelling)			
Sentinel-2	10.07.2017	W (onshore)	5	DF	UA
Sentinel-2	05.07.2017	W (onshore)	9	DF	UA
Sentinel-2	02.07.2017	W (onshore)	3	DF	UA
Sentinel-2	22.06.2017	S	3	UF	DS
Sentinel-2	17.06.2017	(downwelling)			
Sentinel-2	17.06.2017	S	3	UF	DS

Table 3 (continued)

Satellite	Date	Wind direction and type	Wind speed, m/s	Location of the sharp plume front	Plume spreading type
Sentinel-2	13.06.2017	S	3	UF	DS
Landsat 8	06.06.2017	(downwelling)			
Landsat 8	06.06.2017	S	5	UF	DS
Sentinel-2	11.05.2017	(downwelling)			
Sentinel-2	11.05.2017	W (onshore)	3	DF	UA
Sentinel-2	01.05.2017	W (onshore)	3	DF	UA
Landsat 8	26.04.2017	W (onshore)	3	UF	DS
Sentinel-2	11.04.2017	W (onshore)	4	DF	UA
Landsat 8	10.04.2017	S	4	UF	DS
Sentinel-2	08.04.2017	(downwelling)			
Sentinel-2	08.04.2017	S	3	UF	DS
Landsat 8	25.03.2017	(downwelling)			
Landsat 8	25.03.2017	W (onshore)	3	DF	UA
Sentinel-2	12.03.2017	SE	5	UF	DS
Sentinel-2	27.02.2017	(downwelling)			
Sentinel-2	27.02.2017	N (upwelling)	3	UF	DS
Sentinel-2	31.01.2017	E, offshore	1	UF	DS
Sentinel-2	28.01.2017	NE (offshore)	5	UF	DS
Sentinel-2	18.01.2017	NE (offshore)	4	UF	DS
Sentinel-2	22.11.2016	W (onshore)	3	DF	UA
Sentinel-2	19.11.2016	NE (offshore)	5	UF	DS
Landsat 8	01.11.2016	NE (offshore)	5	UF	DS
Sentinel-2	03.10.2016	SE	3	UF	DS
Landsat 8	14.09.2016	(downwelling)			
Landsat 8	14.09.2016	W (onshore)	3	UF	DS
Sentinel-2	13.09.2016	W (onshore)	3	UF	DS
Landsat 8	22.08.2016	W (onshore)	3	UF	DS
Sentinel-2	21.08.2016	W (onshore)	3	UF	DS
Sentinel-2	04.08.2016	0	0	UF	DS
Sentinel-2	01.08.2016	SW (onshore)	4	UF	DS
Landsat 8	28.07.2016	W (onshore)	4	UF	DS
Sentinel-2	15.07.2016	S	3	UF	DS
Sentinel-2	12.06.2016	(downwelling)			
Sentinel-2	12.06.2016	SW (onshore)	3	UF	DS
Landsat 8	25.05.2016	S	5	UF	DS
Landsat 8	09.05.2016	(downwelling)			
Landsat 8	09.05.2016	W (onshore)	4	DF	UA
Sentinel-2	03.05.2016	W (onshore)	3	UF	DS
Landsat 8	02.05.2016	SW (onshore)	3	DF	UA
Sentinel-2	26.04.2016	S	3	UF	DS
Landsat 8	07.04.2016	(downwelling)			
Landsat 8	07.04.2016	S	3	UF	DS
Sentinel-2	06.04.2016	(downwelling)			
Sentinel-2	06.04.2016	S	2	UF	DS
Landsat 8	31.03.2016	(downwelling)			
Landsat 8	31.03.2016	W (onshore)	4	UF	DS
Sentinel-2	13.02.2016	SE	4	UF	DS
Landsat 8	27.01.2016	(downwelling)			
Landsat 8	27.01.2016	NE (offshore)	6	UF	DS
Sentinel-2	18.12.2015	NE (offshore)	5	UF	DS
Landsat 8	17.12.2015	NE (offshore)	5	UF	DS
Landsat 8	30.10.2015	E, offshore	4	UF	DS
Sentinel-2	29.09.2015	W (onshore)	4	UF	DS
Landsat 8	28.09.2015	SE	5	UF	DS
Sentinel-2	19.09.2015	(downwelling)			
Sentinel-2	19.09.2015	W (onshore)	4	UF	DS
Landsat 8	12.09.2015	SW (onshore)	3	UF	DS
Sentinel-2	30.08.2015	W (onshore)	2	DF	UA

Ostrander et al., 2008) and, in particular, on the Mzymta plume (Osadchiv and Zavialov, 2013; Osadchiv, 2015) is significantly lower as compared to wind forcing.

The Mzymta River is characterized by a rapid flow (1–2 m/s), but relatively small depth (1–1.5 m) in the mouth. Therefore, the freshwater jet inflowing to the sea from the Mzymta mouth is characterized by a relatively high speed, but small vertical extent and volume. As a result, it is efficiently decelerated by vertical friction with the subjacent sea water and the initial inertia of the jet decays near the river mouth. A wide range of Mzymta discharge rates (44–118 m³/s) and, therefore, river inflow velocities during the periods considered in this study

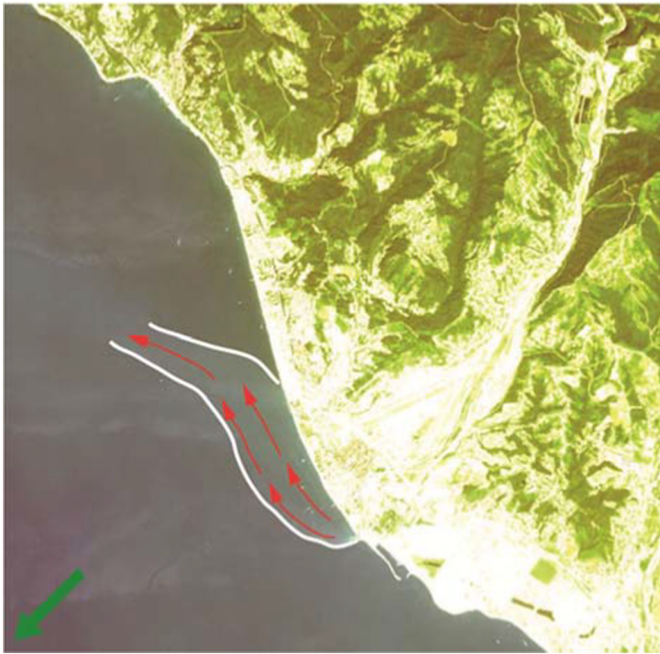


Fig. 6. Sentinel-2 ocean color composite from 27 July 2017 and plume spreading scheme. The white line reproduces the sharp front between the plume and ambient sea, the green arrow indicates wind direction. (For interpretation of the references to color in this figure legend, the reader is referred to the web version of this article.)

resulted in a small range of sizes of the inertia-governed near-field part of the plume (1–2 km) according to the reconstructed surface velocity fields. Thus, the observed spatial scale of the Mzymta near-field plume is of one order of magnitude less than, first, was reported for river plumes formed by rivers with similar discharge rates but lower river inflow velocities (Bourrin et al., 2008; Ostrander et al., 2008; Romero et al., 2016; Zhao et al., 2018), and, second, values numerically estimated by formulae described by Yankovsky and Chapman (1997) and Horner-Devine et al. (2006) based on the Burger and Rossby numbers.

Abrupt deceleration of the near-field jet causes formation of a strong pressure gradient in vicinity of the river mouth, which is directed off the river mouth. As a result, the pressure gradient force hinders anticyclonic recirculation flow directed to the river mouth. Thus, we presume that river discharge volume and inflow velocity are the limiting factors for formation of an anticyclonic bulge within the Mzymta plume during the considered periods of low wind forcing conditions (Fig. 2). This situation is presumed not to occur if a river inflow has a low velocity and/or a large volume and, therefore, is not abruptly decelerated by friction with subjacent sea and does not form strong velocity and pressure gradients in vicinity of the river mouth. However, a detailed study of this factor and its interaction with other conditions that influence near-field dynamics of a small river plume and formation of an anticyclonic bulge (external forcing, estuary width, contact between plume and sea bottom, inflow velocity, Coriolis frequency, and river inflow angle) requires specific in situ measurements and numerical modelling and is beyond this work.

The reconstructed surface velocity fields show strong non-uniformity of average motion directions among different areas of the far-field part of the Mzymta plume in response to wind forcing. The surface layer is moving at an angle of up to 80° to upwelling, onshore, and offshore wind direction in the most stratified parts of the plume adjacent to the Mzymta mouth, while at more mixed outer parts of the plume this angle diminishes to 30–40°. We presume that this effect is caused by inhomogeneity of Ekman layer depth caused by strong variability of stratification at the border between the Mzymta plume and the subjacent sea. This is consistent with the results of numerical

modelling experiments performed by Zhurbas (2013) focused on dependence of parameters of Ekman transport on surface stratification formed by a buoyant river plume. However, to the extent of our knowledge, variability of Ekman angle within a small ocean area, in particular, an individual river plume has not been described before.

Dynamical features of the Mzymta plume described above significantly influence its structure, spreading patterns, and the associated transport of suspended and dissolved river-borne constituents. First, accumulation of freshwater discharge near a river mouth addressed in a number of previous studies (Nof and Pichevin, 2001; Fong and Geyer, 2002; Horner-Devine et al., 2006) does not occur at the Mzymta plume due to small size of its near-field part and absence of a recirculating bulge. As a result, the Mzymta discharge is mainly transported off the river mouth to the wind-driven far-field part of the plume.

Wind forcing induces spreading of a far-field plume in the direction of surface Ekman transport in the coastal sea until it is limited by a coastline. This results in two stable states of a plume defined by the location of a restraining coastline and a river mouth. If plume spreading is limited by a downstream coastline, an alongshore downstream current is formed. Otherwise, if river plume is restrained by an upstream coastline, plume motion decays and it is arrested in this area. These two stable states are generally indicated by upstream/downstream location of a sharp plume front.

Large angles between wind and surface flow directions observed at the strongly stratified part of the Mzymta plume adjacent to the river mouth result in significantly different spreading patterns of the Mzymta plume in response to wind forcing as observed for medium-size and large rivers, especially under onshore and upwelling wind forcing (Fig. 7). Previous works reported that upstream spreading of a river plume is induced by upwelling wind forcing (Geyer et al., 2000; Choi and Wilkin, 2007; Xia et al., 2007). However, upstream spreading and accumulation of the Mzymta plume indicated by downstream location of the sharp plume front was observed only during onshore winds.

Upwelling winds, in contrast, caused intense offshore spreading of freshened water indicated by the largest cross-shore extents of the Mzymta plume, while largest cross-shore scales of medium-size and large river plumes are observed under offshore winds (Xia et al., 2011; Jurisa and Chant, 2012). Downstream propagation of the Mzymta plume as a narrow coastal current under downwelling wind forcing is similar to typical spreading patterns of medium-size and large river plumes (Rennie et al., 1999; Pullen and Allen, 2000; Geyer et al., 2000; Johnson et al., 2001; Choi and Wilkin, 2007).

The spreading area of the Mzymta plume is dominated by offshore and downwelling winds accounting 67% of a year, while onshore winds are registered on average during 18% of a year and 20% during a spring freshet. As a result, the majority of fluvial discharge and river-borne suspended and dissolved matter are directly transported downstream off the river mouth. On the other hand, upstream accumulation of the Mzymta freshwater occurs during a significant part of the year. However, wind forcing in the study region is characterized by high temporal variability. In particular, the duration of the majority of periods of onshore wind forcing is on the order of several hours. Thus, downstream transport of the Mzymta discharge is the dominating spreading pattern of the Mzymta plume, while its long-term upstream accumulation is an infrequent event. This result is consistent with previous studies based on in situ measurements and/or numerical modelling, which showed that terrigenous sediments discharged from small rivers of the study region are transported along the shore and do not accumulate near the estuaries (Dzaoshvili and Papashvili, 1993; Jaoshvili, 2002; Balabanov et al., 2011; Osadchiv and Korshenko, 2017).

5. Summary and conclusions

The present study demonstrates that near simultaneous satellite imagery from Sentinel-2 and Landsat 8 missions can be processed by

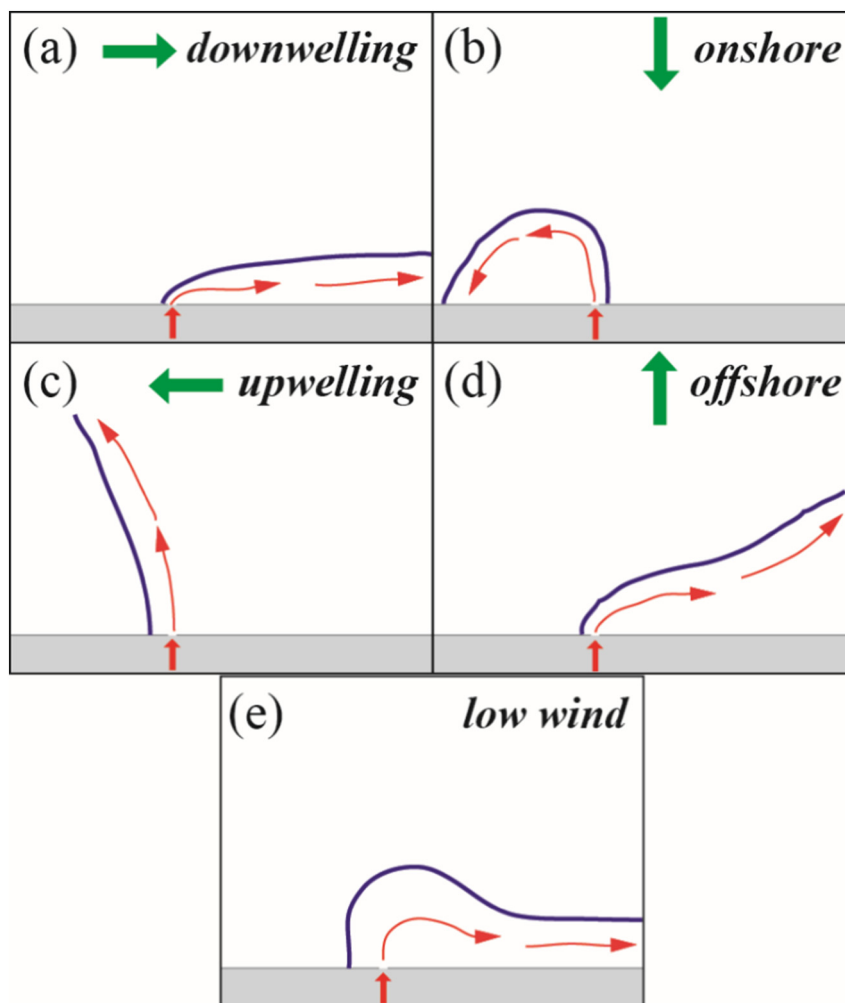


Fig. 7. Schematic of spreading patterns of a small river plume and the related locations of sharp frontal zones of a plume under (a) downwelling, (b) onshore, (c) upwelling, (d) offshore, and (e) low wind forcing conditions.

optical flow algorithms for accurate and precise reconstruction of surface currents in different world regions. Despite relatively sparse temporal coverage of these measurements caused by the long joint repeat cycle of Sentinel-2 and Landsat 8 the reconstructed high resolution snapshots of surface currents hold promise for providing improved qualitative and quantitative insights into various upper ocean current features and dynamics, especially for poorly sampled areas.

In this work we address dynamics of the buoyant plume formed by the Mzymta River located at the northeastern shore of the Black Sea. Using optical flow algorithm we obtained high resolution snapshots of surface velocity fields associated with spreading of the small Mzymta plume under various wind forcing conditions. Based on this data and in situ measurements of local wind and river discharge we obtained new insights into dynamics of small river plumes and identified its differences from dynamics of medium-size and large river plumes.

The low volume of the Mzymta runoff results in low kinetic energy of the near-field jet, which causes its rapid deceleration near the river mouth. As a result, inertia of the river inflow quickly decays, a strong velocity and pressure gradient is formed in vicinity of the river mouth, which hinders formation of an anticyclonic bulge. This fact favors transport of freshwater discharge off the river mouth and its accumulation in the far-field plume under low wind forcing conditions, which is not typical for medium-size and large river plumes.

The reconstructed surface velocity fields showed significant variability of the angle between the wind-induced Ekman transport and wind direction within the Mzymta plume under light and moderate wind

forcing conditions. The angle varied from 30 to 40° at the outer parts of the plume to 60–80° in vicinity of the Mzymta mouth, which is presumably caused by non-homogeneous distribution of surface Ekman layer depth within the river plume. Anomalously large values of angles of Ekman transport observed within the Mzymta plume resulted in significant differences in its spreading patterns in response to wind forcing as compared to large river plumes. In particular, onshore and upwelling wind forcing favored upstream accumulation and offshore transport of the Mzymta plume, respectively. As a result, freshwater discharge of the Mzymta River is transported off the river mouth under upwelling, offshore and downwelling winds, while only onshore wind induces upstream accumulation of freshened water and river-borne nutrients, anthropogenic pollutants, terrigenous sediments, litter near the river mouth.

Frequency, duration, and temporal distribution of wind conditions favorable for formation of upstream/downstream spreading of fluvial water and river-borne suspended and dissolved matter strongly affect local physical, biological, and geochemical processes. In particular, frequent and intense downstream transport of fluvial water can increase salinity anomaly and reduce stratification on long segments of a sea coast (Podymov and Zatsepin, 2016; Osadchiv and Korshenko, 2017). As a result, a river plume can interact with buoyant plumes generated by rivers, whose mouths are located downstream, and influence their structure and dynamics (Mendes et al., 2016; Romero et al., 2016; Warrick and Farnsworth, 2017). On the other hand, long-term upstream accumulation of river-borne nutrients, terrigenous sediments,

anthropogenic pollutants, and litter can significantly impact on local water quality, pollution, food webs, fishery, and engineering activities. Thus, the results obtained in this study, related to influence of along-shore and cross-shore winds on dynamics of small river plumes could be useful for understanding of transport and fate of river-borne constituents delivered by discharge of small rivers, as well as their influence on the marine environment in many world coastal areas.

Data availability

The Landsat 8 Surface Reflectance Level-2 products were downloaded from the United States Geological Survey web repository <http://earthexplorer.usgs.gov> (available after registration). The Sentinel-2 Level-1C products were downloaded from the Copernicus Open Access Hub <https://scihub.copernicus.eu/> (available after registration). The river discharge and wind data were downloaded from the Federal Service for Hydrometeorology and Environmental Monitoring of Russia repositories <http://gis.vodinfo.ru/> (available after registration) and <https://rp5.ru/>.

Competing interests

The authors declare that they have no conflict of interest.

Acknowledgements

This research was funded by the state assignment of FASO Russia, theme 0149-2019-0003 (collecting and processing of satellite imagery), the Russian Ministry of Science and Higher Education, research project 14.W03.31.0006 (application of optical flow algorithms), and the Russian Science Foundation, research project 18-17-00156 (analysis of spreading dynamics of small river plume). The article benefited from critical comments and constructive suggestions from three anonymous reviewers.

References

- Alexeevsky, N.I., Magritsky, D.V., Koltermann, K.P., Krylenko, I.N., Toropov, P.A., 2016. Causes and systematics of inundations of the Krasnodar territory on the Russian Black Sea coast. *Nat. Hazards Earth Syst. Sci.* 16, 1289–1308. <https://doi.org/10.5194/nhess-16-1289-2016>.
- Altena, B., Kaab, A., 2017. Weekly glacier flow estimation from dense satellite time series using adapted optical flow technology. *Front. Earth Sci.* 5, 53. <https://doi.org/10.3389/feart.2017.00053>.
- Avicola, G., Huq, P., 2003. The characteristics of the recirculating bulge region in coastal buoyant outflows. *J. Mar. Res.* 61, 435–463. <https://doi.org/10.1357/002224003322384889>.
- Baker, S., Scharstein, D., Lewis, J., Roth, S., Black, M., Szeliski, R., 2011. A database and evaluation methodology for optical flow. *Int. J. Comput. Vis.* 92, 1–31. <https://doi.org/10.1007/s11263-010-0390-2>.
- Balabanov, I.P., Nikiforov, S.P., Pashkovskiy, I.S., 2011. *Imeretinskaia Lowland. Natural and Geological Conditions, Development Problems, Nedra, Moscow, Russia.* (in Russian).
- Bannehr, L., Rohn, M., Warnecke, G., 1996. A functional analytic method to derive displacement vector fields from satellite image sequences. *Int. J. Remote Sens.* 17 (2), 383–392. <https://doi.org/10.1080/01431169608949013>.
- Bourrin, F., Friend, P.L., Amos, C.L., Manca, E., Ulses, C., Palanques, A., Durrieu De Madron, X., Thompson, C.E.L., 2008. Sediment dispersal from a typical Mediterranean flood: the Têt River, Gulf of Lions. *Cont. Shelf Res.* 28, 1895–1910. <https://doi.org/10.1016/j.csr.2008.06.005>.
- Bowen, M.M., Emery, W.J., Wilkin, J.L., Tildesley, P.C., Barton, I.J., Knewton, R., 2002. Extracting multiyear surface currents from sequential thermal imagery using the maximum cross-correlation technique. *J. Atmos. Ocean. Technol.* 19 (10), 1665–1676. [https://doi.org/10.1175/1520-0426\(2002\)019<1665:EMSCFS>2.0.CO;2](https://doi.org/10.1175/1520-0426(2002)019<1665:EMSCFS>2.0.CO;2).
- Bowman, M.J., Iverson, R.L., 1978. *Estuarine and plume fronts. In: Oceanic Fronts in Coastal Processes.* Springer, Berlin, Heidelberg, pp. 87–104.
- Chant, R.J., Wilkin, J., Zhang, W., Choi, B.-J., Hunter, E., Castela, R., Glenn, S., Jurisa, J., Schofield, O., Houghton, R., Kohut, J., Frazer, T.K., Moline, M.A., 2008. Dispersal of the Hudson River plume in the New York Bight: synthesis of observational and numerical studies during LaTTE. *Oceanography* 21, 148–161. <https://doi.org/10.5670/oceanog.2008.11>.
- Chao, S.Y., Boicort, W.G., 1986. Onset of estuarine plumes. *J. Phys. Oceanogr.* 16, 2137–2149. [https://doi.org/10.1175/1520-0485\(1986\)016<2137:OOEP>2.0.CO;2](https://doi.org/10.1175/1520-0485(1986)016<2137:OOEP>2.0.CO;2).
- Chen, W., 2011. Nonlinear inverse model for velocity estimation from an image sequence. *J. Geophys. Res. Oceans* 116, C6. <https://doi.org/10.1029/2010JC006924>.
- Choi, B.-J., Wilkin, J.L., 2007. The effect of wind on the dispersal of the Hudson River plume. *J. Phys. Oceanogr.* 37, 1878–1897. <https://doi.org/10.1175/JPO3081.1>.
- Devlin, A.T., Pan, J., 2017. *Dynamical estuaries. In: Comprehensive Remote Sensing. Volume 8: Oceans Elsevier, pp. 121–144.*
- Domingues, C.M., Goncalves, G.A., Ghisolfi, R.D., Garcia, C.A.E., 2000. Advective surface velocities derived from sequential infrared images in the southwestern Atlantic Ocean. *Remote Sens. Environ.* 73, 218–226. [https://doi.org/10.1016/S0034-4257\(00\)00096-1](https://doi.org/10.1016/S0034-4257(00)00096-1).
- Dzaoshvili, Sh.V., Papashvili, I.G., 1993. Development and modern dynamics of alluvial-accumulative coasts of the eastern Black sea. *In: Coastlines of the Black Sea. ASCE, New-York, pp. 224–233.*
- Emery, W.J., Thomas, A.C., Collins, M.J., Crawford, W.R., Mackas, D.L., 1986. An objective method for computing advective surface velocities from sequential infrared satellite images. *J. Geophys. Res.* 91 (C11), 12865–12878. <https://doi.org/10.1029/JC091iC11p12865>.
- Emery, W.J., Fowler, C., Clayson, C.A., 1992. Satellite-image-derived Gulf Stream currents compared with numerical model results. *J. Atmos. Ocean. Technol.* 9, 286–304. [https://doi.org/10.1175/1520-0426\(1992\)009<0286:SIDGSC>2.0.CO;2](https://doi.org/10.1175/1520-0426(1992)009<0286:SIDGSC>2.0.CO;2).
- Emmett, R.L., Krutzikowsky, G.K., Bentley, P., 2006. Abundance and distribution of pelagic piscivorous fishes in the Columbia River plume during spring/early summer 1998–2003: relationship to oceanographic conditions, forage fishes, and juvenile salmonids. *Prog. Oceanogr.* 68, 1–26. <https://doi.org/10.1016/j.pocean.2005.08.001>.
- Farneback, G., 2003. Two-frame motion estimation based on polynomial expansion. *In: Bigun, J., Gustavsson, T. (Eds.), Image Analysis, SCIA 2003, 363–370. Lecture Notes in Computer Science, vol. 2749 Springer, Berlin, Heidelberg. https://doi.org/10.1007/3-540-45103-X_50.*
- Fong, D.A., Geyer, W.R., 2001. Response of a river plume during an upwelling favorable wind event. *J. Geophys. Res.* 106, 1067–1084. <https://doi.org/10.1029/2000jc900134>.
- Fong, D.A., Geyer, W.R., 2002. The alongshore transport of freshwater in a surface-trapped river plume. *J. Phys. Oceanogr.* 32, 957–972. [https://doi.org/10.1175/1520-0485\(2002\)032<0957:tatofi>2.0.co;2](https://doi.org/10.1175/1520-0485(2002)032<0957:tatofi>2.0.co;2).
- Fortun, D., Boutheymy, P., Kervrann, C., 2015. Optical flow modeling and computation: a survey. *Comput. Vis. Image Underst.* 134, 1–21. <https://doi.org/10.1016/j.cviu.2015.02.008>.
- Geyer, W.R., Hill, P., Milligan, T., Traykovski, P., 2000. The structure of the Eel River plume during floods. *Cont. Shelf Res.* 20, 2067–2093. [https://doi.org/10.1016/S0278-4343\(00\)00063-7](https://doi.org/10.1016/S0278-4343(00)00063-7).
- Hetland, R.D., Hsu, T.-J., 2013. *Freshwater and sediment dispersal in large river plumes. In: Bianchi, T.S., Allison, M.A., Cai, W.-J. (Eds.), Biogeochemical Dynamics at Large River-Coastal Interfaces: Linkages with Global Climate Change. Springer, New York, pp. 55–85.*
- Horn, B.K.P., Schunck, B.G., 1981. Determining optical flow. *Artif. Intell.* 17, 185–203.
- Horner-Devine, A.R., 2009. The bulge circulation in the Columbia River plume. *Cont. Shelf Res.* 29, 234–251. <https://doi.org/10.1016/j.csr.2007.12.012>.
- Horner-Devine, A.R., Fong, D.A., Monismith, S.G., Maxworthy, T., 2006. Laboratory experiments simulating a coastal river discharge. *J. Fluid Mech.* 555, 203–232. <https://doi.org/10.1017/s0022112006008937>.
- Horner-Devine, A.R., Hetland, R.D., MacDonald, D.G., 2015. Mixing and transport in coastal river plumes. *Annu. Rev. Fluid Mech.* 47, 569–594. <https://doi.org/10.1146/annurev-fluid-1010313-141408>.
- Hu, Z., Wang, D.-P., Pan, D., He, X., Miyazawa, Y., Bai, Y., Wang, D., Gong, F., 2016. Mapping surface tidal currents and Changjiang plume in the East China Sea from Geostationary Ocean Color Imager. *J. Geophys. Res. Oceans* 121, 1563–1572. <https://doi.org/10.1002/2015JC011469>.
- Huang, W.J., Cai, W.J., Wang, Y., Lohrenz, S.E., Murrell, M.C., 2015. The carbon dioxide system on the Mississippi River-dominated continental shelf in the northern Gulf of Mexico: 1. Distribution and air-sea CO₂ flux. *J. Geophys. Res. Oceans* 120, 1429–1445. <https://doi.org/10.1002/2014jc010498>.
- Jaoshvili, S. (Ed.), 2002. *The Rivers of the Black Sea. Chimeriki, I., Gigineishvili, G., Kordzadze, A. (Eds.), 2002. Technical Report No. 71 European Environmental Agency.*
- Jay, D.A., Pan, J., Orton, P.M., Horner-Devine, A.R., 2009. Asymmetry of Columbia River tidal plume fronts. *J. Mar. Syst.* 78, 442–459. <https://doi.org/10.1016/j.jmarsys.2008.11.015>.
- Johnson, D., Weidemann, A., Arnone, R., Davis, C., 2001. Chesapeake Bay outflow plume and coastal upwelling events: physical and optical properties. *J. Geophys. Res.* 106 (C6), 11613–11622. <https://doi.org/10.1029/1999JC000185>.
- Jurisa, J.T., Chant, R., 2012. The coupled Hudson River estuarine-plume response to variable wind and river forcings. *Ocean Dyn.* 62 (5), 771–784. <https://doi.org/10.1007/s10236-012-0527-7>.
- Korotenko, K.A., Osadchiv, A.A., Zavialov, P.O., Kao, R.-C., Ding, C.-F., 2014. Effects of bottom topography on dynamics of river discharges in tidal regions: case study of twin plumes in Taiwan Strait. *Ocean Sci.* 10, 865–879. <https://doi.org/10.5194/os-10-863-2014>.
- Korotkina, O.A., Zavialov, P.O., Osadchiv, A.A., 2011. Submesoscale variability of the current and wind fields in the coastal region of Sochi. *Oceanology* 51, 745–754. <https://doi.org/10.1134/s0001437011050109>.
- Korotkina, O.A., Zavialov, P.O., Osadchiv, A.A., 2014. Synoptic variability of currents in the coastal waters of Sochi. *Oceanology* 54, 545–556. <https://doi.org/10.1134/s0001437014040079>.
- Kubryakov, A.A., Stanichny, S.V., Zatssepina, A.G., 2018. Interannual variability of Danube

- waters propagation in summer period of 1992–2015 and its influence on the Black Sea ecosystem. *J. Mar. Syst.* 179, 10–30. <https://doi.org/10.1016/j.jmarsys.2017.11.001>.
- Kudela, R.M., Horner-Devine, A.R., Banas, N.S., Hickey, B.M., Peterson, T.D., Lessard, E.J., Frame, E., Bruland, K.W., Lohan, M., Jay, D.A., Peterson, J., Peterson, B., Kosro, M., Palacios, S., Dever, E.P., 2010. Multiple trophic levels fueled by recirculation in the Columbia River plume. *Geophys. Res. Lett.* 37, L18607. <https://doi.org/10.1029/2010GL044342>.
- Lenzano, M.G., Lannutti, E., Toth, C., Rivera, A., Lenzano, L., 2018. Detecting glacier surface motion by optical flow. *Photogramm. Eng. Remote Sens.* 84, 33–42. <https://doi.org/10.14358/PERS.84.1.33>.
- Li, J., Roy, D.P., 2017. A global analysis of Sentinel-2A, Sentinel-2B and Landsat-8 data revisit intervals and implications for terrestrial monitoring. *Remote Sens.* 9, 902. <https://doi.org/10.3390/rs9090902>.
- Liu, Y., MacCready, P., Hickey, B.M., Dever, E.P., Kosro, P.M., Banas, N.S., 2009. Evaluation of a coastal ocean circulation model for the Columbia River plume in summer 2004. *J. Geophys. Res.* 114, C00B04. <https://doi.org/10.1029/2008gl036447>.
- Lucas, B., Kanade, T., 1981. An iterative image registration technique with an application to stereo vision. In: *Proceedings of Imaging Understanding Workshop*, pp. 121–130.
- MacDonald, D.G., Goodman, L., Hetland, R.D., 2007. Turbulent dissipation in a near-field river plume: a comparison of control volume and microstructure with a numerical model. *J. Geophys. Res.* 112, C07026. <https://doi.org/10.1029/2006JC004075>.
- Marcello, J., Eugenio, F., Marques, F., Hernandez-Guerra, A., Gasull, A., 2008. Motion estimation techniques to automatically track oceanographic thermal structures in multisensor image sequences. *IEEE Trans. Geosci. Remote Sens.* 46 (9), 2743–2762. <https://doi.org/10.1109/TGRS.2008.919274>.
- Mathews, D.K., Emery, W.J., 2009. Velocity observations of the California Current derived from satellite imagery. *J. Geophys. Res.* 114 (C8). <https://doi.org/10.1029/2008JC005029>.
- Medvedev, I.P., 2018. Tides in the Black Sea: observations and numerical modelling. *Pure Appl. Geophys.* 1–19. <https://doi.org/10.1007/s00024-018-1878-x>.
- Medvedev, I.P., Rabinovich, A.B., Kulikov, E.A., 2016. Tides in three enclosed basins: the Baltic, Black, and Caspian seas. *Front. Mar. Sci.* 3, 1–7. <https://doi.org/10.3389/fmars.2016.00046>.
- Mendes, R., Sousa, M.C., Maite, D., Gomez-Gesteira, M., Dias, J.M., 2016. New insights into the Western Iberian Buoyant Plume: interaction between the Douro and Minho River plumes under winter conditions. *Prog. Oceanogr.* 141, 30–43. <https://doi.org/10.1016/j.pocean.2015.11.006>.
- Mercatini, A., Griffo, A., Piterberg, L., Zambianchi, Z., Magaldi, M.G., 2010. Estimating surface velocities from satellite data and numerical models: implementation and testing of a new simple method. *Ocean Model* 33, 190–203. <https://doi.org/10.1016/j.oceanmod.2010.01.003>.
- Milliman, J.D., Svytski, J.P.M., 1992. Geomorphic-tectonic control of sediment discharge to the ocean: the importance of small mountainous rivers. *J. Geol.* 100, 525–544. <https://doi.org/10.1086/629606>.
- Milliman, J.D., Farnsworth, K.L., Albertin, C.S., 1999. Flux and fate of fluvial sediments leaving large islands in the East Indies. *J. Sea Res.* 41, 97–107. [https://doi.org/10.1016/S1385-1101\(98\)00040-9](https://doi.org/10.1016/S1385-1101(98)00040-9).
- Milliman, J.D., Lin, S.W., Kao, S.J., Liu, J.P., Liu, C.S., Chiu, J.K., Lin, Y.C., 2007. Short-term changes in seafloor character due to flood-derived hyperpycnal discharge: typhoon Mindulle, Taiwan, July 2004. *Geology* 35, 779–782. <https://doi.org/10.1130/G23760A.1>.
- Nezlin, N.P., DiGiacomo, P.M., 2005. Satellite ocean color observations of stormwater runoff plumes along the San Pedro Shelf (southern California) during 1997 to 2003. *Cont. Shelf Res.* 25, 1692–1711. <https://doi.org/10.1016/j.csr.2005.05.001>.
- Nezlin, N.P., DiGiacomo, P.M., Stein, E.D., Ackerman, D., 2005. Stormwater runoff plumes observed by SeaWiFS radiometer in the Southern California Bight. *Remote Sens. Environ.* 98, 494–510. <https://doi.org/10.1016/j.rse.2005.08.008>.
- Nof, D., Pichevin, T., 2001. The ballooning of outflows. *J. Phys. Oceanogr.* 31, 3045–3058. [https://doi.org/10.1175/1520-0485\(2001\)031<3045:tboo>2.0.co;2](https://doi.org/10.1175/1520-0485(2001)031<3045:tboo>2.0.co;2).
- O'Donnell, J., 1990. The formation and fate of a river plume: a numerical model. *J. Phys. Oceanogr.* 20, 551–569. [https://doi.org/10.1175/1520-0485\(1990\)020<0551:TFAFOA>2.0.CO;2](https://doi.org/10.1175/1520-0485(1990)020<0551:TFAFOA>2.0.CO;2).
- O'Donnell, J., 2010. The dynamics of estuary plumes and fronts. In: Valle Levinson, A. (Ed.), *Contemporary Issues in Estuarine Physics*. Cambridge Univ. Press, Cambridge, UK, pp. 186–246.
- O'Donnell, J., Marmorino, G.O., Trump, C.L., 1998. Convergence and downwelling at a river plume front. *J. Phys. Oceanogr.* 28, 1481–1495.
- O'Donnell, J., Ackleson, S.G., Levine, E.R., 2008. On the spatial scales of a river plume. *J. Geophys. Res. Oceans* 113, C4. <https://doi.org/10.1029/2007JC004440>.
- Osadchiv, A.A., 2015. A method for quantifying freshwater discharge rates from satellite observations and Lagrangian numerical modeling of river plumes. *Environ. Res. Lett.* 10, 085009. <https://doi.org/10.1088/1748-9326/10/8/085009>.
- Osadchiv, A.A., 2018. Small mountainous rivers generate high-frequency internal waves in coastal ocean. *Sci. Rep.* 8, 16609. <https://doi.org/10.1038/s41598-018-35070-7>.
- Osadchiv, A., Korshenko, E., 2017. Small river plumes off the northeastern coast of the Black Sea under average climatic and flooding discharge conditions. *Ocean Sci.* 13, 465–482. <https://doi.org/10.5194/os-13-465-2017>.
- Osadchiv, A.A., Zavialov, P.O., 2013. Lagrangian model for surface-advected river plume. *Cont. Shelf Res.* 58, 96–106. <https://doi.org/10.1016/j.csr.2013.03.010>.
- Osadchiv, A.A., Korotenko, K.A., Zavialov, P.O., Chiang, W.-S., Liu, C.-C., 2016. Transport and bottom accumulation of fine river sediments under typhoon conditions and associated submarine landslides: case study of the Peinan River, Taiwan. *Nat. Hazards Earth Syst. Sci.* 16, 41–54. <https://doi.org/10.5194/nhess-16-41-2016>.
- Osadchiv, A.A., Izhitskiy, A.S., Zavialov, P.O., Kremenetskiy, V.V., Polukhin, A.A., Pelevin, V.V., Toktamysova, Z.M., 2017. Structure of the buoyant plume formed by Ob and Yenisei river discharge in the southern part of the Kara Sea during summer and autumn. *J. Geophys. Res. Oceans* 122. <https://doi.org/10.1002/2016JC012603>.
- Ostrander, C.E., McManus, M.A., Decarlo, E.H., Mackenzie, F.T., 2008. Temporal and spatial variability of freshwater plumes in a semi-enclosed estuarine-bay system. *Estuar. Coasts* 31, 192–203. <https://doi.org/10.1007/s12237-007-9001-z>.
- Petrou, Z.I., Tian, Y., 2017. High-resolution sea ice motion estimation with optical flow using satellite spectroradiometer data. *IEEE Trans. Geosci. Remote Sens.* 55, 1339–1350. <https://doi.org/10.1109/TGRS.2016.2622714>.
- Podymov, O.I., Zatssepina, A.G., 2016. Seasonal anomalies of water salinity in the Gelendzhik region of the Black Sea according to shipborne monitoring data. *Oceanology* 56 (3), 342–354. <https://doi.org/10.1134/S0001437016020156>.
- Pullen, J.D., Allen, J.S., 2000. Modeling studies of the coastal circulation off northern California: shelf response to a major eel river flood event. *Cont. Shelf Res.* 20, 2213–2238. [https://doi.org/10.1016/S0278-4343\(00\)00068-6](https://doi.org/10.1016/S0278-4343(00)00068-6).
- Rabalais, N.N., 2010. Eutrophication of estuarine and coastal ecosystems. In: Mitchell, R., Gu, J.-D. (Eds.), *Environmental Microbiology*, 2nd edition. Wiley, Hoboken, NJ, pp. 115–134.
- Rennie, S.E., Largier, J.L., Lentz, S.J., 1999. Observations of a pulsed buoyancy current downstroke of Chesapeake Bay. *J. Geophys. Res.* 104 (C8), 18227–18240. <https://doi.org/10.1029/1999JC000153>.
- Romero, L., Siegel, D.A., McWilliams, J.C., Uchiyama, Y., Jones, C., 2016. Characterizing storm water dispersion and dilution from small coastal streams. *J. Geophys. Res. Oceans* 121, 3926–3943. <https://doi.org/10.1002/2015JC011323>.
- Saldias, G.S., Sobarzo, M., Largier, J., Moffat, C., Letelier, R., 2012. Seasonal variability of turbid river plumes off central Chile based on high-resolution MODIS imagery. *Remote Sens. Environ.* 123, 220–233. <https://doi.org/10.1016/j.rse.2012.03.010>.
- Simpson, J.H., 1997. Physical processes in the ROFI regime. *J. Mar. Syst.* 12, 3–15. [https://doi.org/10.1016/S0924-7963\(96\)00085-1](https://doi.org/10.1016/S0924-7963(96)00085-1).
- Soosaar, E., Maljutenko, I., Uiboupin, R., Skudra, M., Raudsepp, U., 2016. River bulge evolution and dynamics in a non-tidal sea – Daugava River plume in the Gulf of Riga, Baltic Sea. *Ocean Sci.* 12, 417–432. <https://doi.org/10.5194/os-12-417-2016>.
- Storey, J., Roy, D.P., Masek, J., Gascon, F., Dwyer, J., Choate, M., 2016. A note on the temporary misregistration of Landsat-8 Operational Land Imager (OLI) and Sentinel-2 Multi Spectral Instrument (MSI) imagery. *Remote Sens. Environ.* 186, 121–122. <https://doi.org/10.1016/j.rse.2016.08.025>.
- Sun, H., Song, Q., Shao, R., Schlicke, T., 2016. Estimation of sea surface currents based on ocean colour remote-sensing image analysis. *Int. J. Remote Sens.* 37 (21), 5105–5121. <https://doi.org/10.1080/01431161.2016.1226526>.
- Thomas, P.J., Linden, P.F., 2007. Rotating gravity currents: small-scale and large-scale laboratory experiments and a geostrophic model. *J. Fluid Mech.* 578, 35–65. <https://doi.org/10.1017/s0022112007004739>.
- Thomas, A., Weatherbee, R.A., 2006. Satellite-measured temporal variability of the Columbia River plume. *Remote Sens. Environ.* 100, 167–178. <https://doi.org/10.1016/j.rse.2005.10.018>.
- Trump, C.L., Marmorino, G.O., 2003. Mapping small-scale along-front structure using ADCP acoustic backscatter range-bin data. *Estuaries* 26, 878–884. <https://doi.org/10.1007/BF02803346>.
- Warrick, J.A., Farnsworth, K.L., 2017. Coastal river plumes: collisions and coalescence. *Prog. Oceanogr.* 151, 245–260. <https://doi.org/10.1016/j.pocean.2016.11.008>.
- Warrick, J.A., Mertes, L.A.K., Washburn, L., Siegel, D.A., 2004. Dispersal forcing of southern California river plumes, based on field and remote sensing observations. *Geo-Mar. Lett.* 24, 46–52. <https://doi.org/10.1007/s00367-003-0163-9>.
- Warrick, J.A., DiGiacomo, P.M., Weisberg, S.B., Nezlin, N.P., Mengel, M., Jones, B.H., Ohlmann, J.C., Washburn, L., Terrill, E.J., Farnsworth, K.L., 2007. River plume patterns and dynamics within the Southern California Bight. *Cont. Shelf Res.* 27 (19), 2427–2448. <https://doi.org/10.1016/j.csr.2007.06.015>.
- Washburn, L., McClure, K.A., Jones, B.H., Bay, S.M., 2003. Spatial scales and evolution of stormwater plumes in Santa Monica Bay. *Mar. Environ. Res.* 56, 103–125. [https://doi.org/10.1016/S0141-1136\(02\)00327-6](https://doi.org/10.1016/S0141-1136(02)00327-6).
- Whitney, M.M., Garvine, R.W., 2005. Wind influence on a coastal buoyant outflow. *J. Geophys. Res.* 110, C03014. <https://doi.org/10.1029/2003JC002261>.
- Wu, Q., Wang, H.Q., Lin, Y.J., Zhuang, Y.Z., Zhang, Y., 2016. Deriving AMVs from geostationary satellite images using optical flow algorithm based on polynomial expansion. *J. Atmos. Ocean. Technol.* 33, 1727–1747. <https://doi.org/10.1175/JTECH-D-16-0013.1>.
- Xia, M., Xie, L., Pietrafesa, L.J., 2007. Modeling of the Cape Fear River estuary plume. *Estuar. Coasts* 30, 698–709. <https://doi.org/10.1007/BF02841966>.
- Xia, M., Xie, L., Pietrafesa, L.J., Whitney, M.M., 2011. The ideal response of a Gulf of Mexico estuary plume to wind forcing: its connection with salt flux and a Lagrangian view. *J. Geophys. Res. Oceans* 116, C08035. <https://doi.org/10.1029/2010JC006689>.
- Yang, H., Choi, J.-K., Park, Y.-J., Han, H.-J., Ryu, J.-H., 2014. Application of the Geostationary Ocean Color Imager (GOCI) to estimates of ocean surface currents. *J. Geophys. Res. Oceans* 119, 3988–4000. <https://doi.org/10.1002/2014JC009981>.
- Yang, H., Arnore, R., Jolliff, J., 2015. Estimating advective near-surface currents from ocean color satellite images. *Remote Sens. Environ.* 158, 1–14. <https://doi.org/10.1016/j.rse.2014.11.010>.
- Yankovsky, A.E., Chapman, D.C., 1997. A simple theory for the fate of buoyant coastal discharges. *J. Phys. Oceanogr.* 27, 1386–1401. [https://doi.org/10.1175/1520-0485\(1997\)027<1386:astfft>2.0.co;2](https://doi.org/10.1175/1520-0485(1997)027<1386:astfft>2.0.co;2).
- Yankovsky, A.E., Hickey, B.M., Münchow, A.K., 2001. Impact of variable inflow on the dynamics of a coastal buoyant plume. *J. Geophys. Res. Oceans* 106 (C9), 19809–19824. <https://doi.org/10.1029/2001JC000792>.
- Yuan, Y., Horner-Devine, A.R., Avener, M., Bevan, S., 2018. The role of periodically varying discharge on river plume structure and transport. *Cont. Shelf Res.* 158,

- 15–25. <https://doi.org/10.1016/j.csr.2018.02.009>.
- Zavialov, P.O., Grigorieva, J.V., Möller, O.O., Kostianoy, A.G., Gregoire, M., 2002. Continuity preserving modified maximum cross-correlation technique. *J. Geophys. Res. Oceans* 107 (C10), 3160. <https://doi.org/10.1029/2001JC001116>.
- Zavialov, P.O., Makkaveev, P.N., Konovalov, B.V., Osadchiev, A.A., Khlebopashev, P.V., Pelevin, V.V., Grabovskiy, A.B., Izhitskiy, A.S., Goncharenko, I.V., Soloviev, D.M., Polukhin, A.A., 2014. Hydrophysical and hydrochemical characteristics of the sea areas adjacent to the estuaries of small rivers of the Russian coast of the Black Sea. *Oceanology* 54, 265–280. <https://doi.org/10.1134/s0001437014030151>.
- Zhao, J., Gong, W., Shen, J., 2018. The effect of wind on the dispersal of a tropical small river plume. *Front. Earth Sci.* 12, 170–190. <https://doi.org/10.1007/s11707-016-0628-6>.
- Zhou, M.-J., Shen, Z.-L., Yu, R.-C., 2008. Responses of a coastal phytoplankton community to increased nutrient input from the Changjiang (Yangtze) River. *Cont. Shelf Res.* 28, 1483–1489. <https://doi.org/10.1016/j.csr.2007.02.009>.
- Zhurbas, N.V., 2013. The wind-induced drift velocity of the freshwater layer on the sea's surface. *Oceanology* 53, 136–144. <https://doi.org/10.1134/s0001437013020161>.